



Sensor-based Autonomous Navigation of Omnidirectional Vehicles Dealing with Collisions and Occlusions in Unknown Environments

Abdellah Khelloufi, Nouara Achour, Robin Passama, Andrea Cherubini

► To cite this version:

Abdellah Khelloufi, Nouara Achour, Robin Passama, Andrea Cherubini. Sensor-based Autonomous Navigation of Omnidirectional Vehicles Dealing with Collisions and Occlusions in Unknown Environments. 2017. hal-01625946v1

HAL Id: hal-01625946

<https://hal.science/hal-01625946v1>

Preprint submitted on 30 Oct 2017 (v1), last revised 20 May 2019 (v5)

HAL is a multi-disciplinary open access archive for the deposit and dissemination of scientific research documents, whether they are published or not. The documents may come from teaching and research institutions in France or abroad, or from public or private research centers.

L'archive ouverte pluridisciplinaire **HAL**, est destinée au dépôt et à la diffusion de documents scientifiques de niveau recherche, publiés ou non, émanant des établissements d'enseignement et de recherche français ou étrangers, des laboratoires publics ou privés.

Sensor-based Navigation of Omnidirectional Robots Dealing with both Collisions and Occlusions in Unknown Environments

Abdellah Khelloufi, Nouara Achour, Robin Passama, Andrea Cherubini

Abstract—Navigation tasks are often subject to several constraints that can be related to the sensors (visibility) or come from the environment (obstacles). In this paper, we propose a framework for omnidirectional mobile robots that takes into account both collision and occlusion risk, during sensor-based navigation. The task consists in driving the robot towards a visual target in the presence of static and moving obstacles. The target is acquired by fixed —*limited field of view*— on-board sensors, while the obstacles surrounding the robot are detected by lidar scanners. To perform the task, the robot has not only to keep the target in view while avoiding the obstacles, but also to predict its location in the case of occlusion. The effectiveness of our approach is validated through several simulated and real experiments.

Index Terms—Sensor-based navigation, obstacle avoidance, visibility constraints, occlusions.

I. INTRODUCTION

NAVIGATION strategies generally aim at endowing a mobile robot with capacities of perception, decision, and action, that allow it to autonomously navigate in the environment. These strategies are traditionally divided in two main classes, depending on whether the problem is solved *locally* or *globally*. The *global* approach [1], [2], usually consists in motion planning, hence relies on accurate knowledge of the robot pose and on a global map of the environment. On the other hand, *local* or reactive strategies are based on instantaneous information acquired by the robot sensors. These strategies include: potential fields [3], vector field histogram [4], elastic band [5], dynamic window [6], obstacle-restriction method [7], and closest gap [8].

One of the advantages of reactive strategies is that they can be well combined with other sensor-based approaches such as visual servoing [9], [10]. In visual servoing, the task is defined in the sensor space, instead of configuration space, and it does not require neither a global model of the environment nor robot localization. Works in this area include [11], where image-based navigation is combined with obstacle avoidance, for a

differential-drive robot equipped with a pan actuated camera. Moving obstacles may be considered in the same approach, as shown in [12]. Recently, another interesting framework for visual navigation with obstacle avoidance has been presented in [13], for a car-like robot equipped with an actuated camera and a lidar. The framework is based on tentacles [16], [17], i.e., drivable paths used to predict possible collisions in the near future. The task realized in [13] consists in following a visual path represented by key images, without colliding with the ground obstacles. The authors show that obstacle avoidance does not affect the visual navigation performance. Furthermore, the approach presents many advantages over potential fields, as shown in [14]. The framework was later improved [15], by using a Kalman filter to deal with obstacles moving during navigation.

A frequent problem in vision-based task control is the loss of image features, due to occlusions or to the sensor's limited field of view. Various prediction and correction methods have been proposed to solve this issue [18]–[23]. However, all these approaches are dedicated to manipulator arms. In the context of mobile robotics, the problem of keeping visual target or landmark visibility has been addressed from different viewpoints. The authors of [24] and [25] study the shortest paths in terms of distance in the image plane for a differential drive robot equipped with a limited field of view sensor. The objective is to obtain the globally optimal paths that allow the robot to maintain a landmark in sight in the absence of obstacles. Recently, these works have been extended to handle environments populated with static obstacles [26]–[28]. However, all the methods proposed in these works are based on motion planning and require a priori knowledge of the robot environment. On the other hand, some researchers have addressed visibility constraints in reactive, purely sensor-based navigation strategies. For example, in [29], a homography-based visual servo controller drives a mobile robot to a goal pose by following some of the optimal paths proposed in [24]. Another solution, proposed in [30], consists in predicting the location of features, when they are not visible, during visual navigation in the presence of static obstacles.

Another limitation of the works presented above is that none addresses control of omnidirectional mobile robots. These systems, however, are getting increasingly popular in industrial applications, since they can perform complex three-dimensional trajectories in the plane, indispensable in limited footprint environments. It is therefore surprising that no attention has been paid to incorporating collision and occlusion

A. Khelloufi is with the Center for Development of Advanced Technologies CDTA, 20 Aout 1956 City, Baba Hassen Algiers, Algeria. (e-mail: akhelloufi@cdta.dz) and with the Faculty of Electronics and Computer Science, University of Sciences and Technology Houari Boumediene USTHB, BP32 EL-ALIA, 16111 Bab Ezzouar Algiers, Algeria.

N. Achour is with the Faculty of Electronics and Computer Science, University of Sciences and Technology Houari Boumediene USTHB, BP32 EL-ALIA, 16111 Bab Ezzouar Algiers, Algeria. (e-mail: nachour@usthb.dz)

R. Passama and A. Cherubini are with the Laboratory for Computer Science, Micro-electronics and Robotics LIRMM - Université de Montpellier CNRS, 161 Rue Ada, 34090 Montpellier, France. (e-mail: lastname@lirmm.fr)

Manuscript received XX; revised xx.

constraints in the navigation tasks of such platforms.

In this paper, we address the problem of dealing with both collisions and occlusions caused by static and moving obstacles, during visual navigation of an omnidirectional mobile robot equipped with fixed —*limited field of view*— on-board sensors. Specifically, the navigation task consists in safely driving the robot towards a static or moving target, in an unknown environment. The robot has to avoid the obstacles and to maintain the target in its field of view, while simultaneously handling partial or total occlusions.

To solve this problem, we propose a generalization of the framework designed in [13] for car-like robots, by introducing *omnidirectional tentacles*. These tentacles are characterized not only by curvature, but also by course angle, since the robot linear velocity is not necessarily aligned with the robot heading, as in traditional nonholonomic systems. We also consider the visibility constraints that are induced by the limitations of the fixed sensors field of view. Furthermore, if the target is lost or (partially or totally) occluded by an obstacle, a fast and efficient strategy is designed to estimate its current pose, by using its previous pose along with the control inputs.

Let us summarize the constraints that are satisfied by our approach: 1) the robot safety is ensured, by avoiding collisions with static and moving obstacles, 2) the target is maintained as much as possible within the sensors field of view even in presence of obstacles, 3) the loss or occlusion of the target is handled by continuous online estimation of its pose.

To our knowledge, this is the first work addressing and validating experimentally safe sensor-based navigation of omnidirectional robots under these three constraints. A very preliminary version of our framework was presented in [31] without considering target occlusion problem nor real vision (the target pose was estimated via odometry alone). Our main contributions with regards to that work are indicated hereby.

- The development of an algorithm for detecting and tracking the target pose, using one or two cameras along with the lidar measures.
- The inclusion of target loss management to deal simultaneously with collision and occlusion.
- Analytical proofs of the conditions for controller asymptotic stability.
- Independence of the framework from odometry data.

The remainder of the paper is organized as follows. In Sect. II, the problem and relevant variables are defined. The omnidirectional generalization of tentacles is presented in Sect. III, and we detail our controller in Sect. IV. In Sect. V, we present the strategy for determining the best path (tentacle) for navigation. Section VI describes the algorithm used to detect and track the visual target. Simulated and real experiments are presented in Sect. VII, and we finally conclude in Sect. VIII.

II. GENERAL DEFINITIONS

A. Robotic platform

We consider an omnidirectional mobile robot, which can move in any direction on the ground plane. Hence, the control

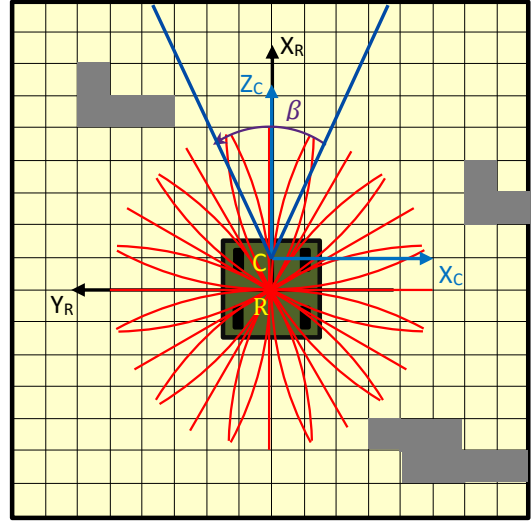


Fig. 1. General definitions. The robot frame \mathcal{F}_R is shown along with the occupancy grid (yellow), occupied cells (gray), omnidirectional tentacles (red), and visual sensor center (C) with its field of view (blue).

inputs are:

$$\mathbf{u} = [v_X \ v_Y \ \omega]^\top. \quad (1)$$

These are aligned with the axes of the robot frame $\mathcal{F}_R(R, X_R, Y_R)$ (see Fig. 1), with R the robot center of rotation, X_R pointing forward and Y_R pointing left.

The robot is equipped with a set of forward looking visual sensors (e.g., one or more cameras) with a combined field of view β , centered at C . It also has distance sensors for building a local map (occupancy grid) of the obstacles surrounding it. The visual sensors are fixed, so the robot heading also determines its viewing direction.

B. Visual target

The task to be performed by the robot consists in driving towards a visible target, while avoiding the environment obstacles. When the environment is safe, the robot should progress forward, while viewing the target. In case avoidable obstacles (either static or moving) are present, the robot should circumnavigate them, while maintaining the target in the field of view. If the target is lost or occluded by an obstacle, its current pose must be estimated by using its previous location along with the current robot control inputs. Finally, if collision is inevitable or if the target is not visible for a long time, the robot must stop.

The specifications of the navigation task are:

- 1) orient the robot so as to point the visual sensors towards the target,
- 2) make the robot progress towards the target,
- 3) avoid collisions with the obstacles, while keeping the target in sight.
- 4) estimate the target pose during occlusions, in order to predict its pose in case of reappearance.

More formally, to fulfill specification 2, the robot should be controlled so that the visual target T (that can be static or moving) is displaced in \mathcal{F}_R , from the current pose

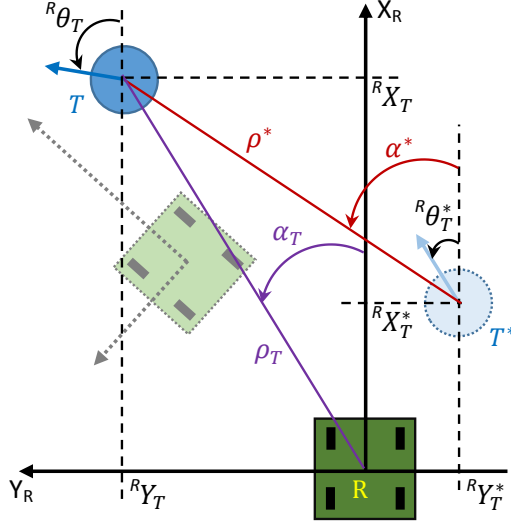


Fig. 2. Definition of the visual task variables.

${}^R \mathbf{p}_T = [{}^R X_T \ {}^R Y_T \ {}^R \theta_T]^\top$ to a desired *constant* pose, ${}^R \mathbf{p}_T^* = [{}^R X_T^* \ {}^R Y_T^* \ {}^R \theta_T^*]^\top$ (see Fig. 2 for a complete illustration of these variables).

We define (see Fig. 2):

- 1) the *distance between current and desired target positions*:

$$\rho^* = \sqrt{({}^R X_T - {}^R X_T^*)^2 + ({}^R Y_T - {}^R Y_T^*)^2}, \quad (2)$$

- 2) the *orientation offset between current and desired target positions*, defined only when $\rho^* \neq 0$:

$$\alpha^* = \text{atan2}({}^R Y_T - {}^R Y_T^*, {}^R X_T - {}^R X_T^*), \quad (3)$$

- 3) the *distance between robot and target position*:

$$\rho_T = \sqrt{{}^R X_T^2 + {}^R Y_T^2}, \quad (4)$$

- 4) the *heading to the target*:

$$\alpha_T = \begin{cases} \text{atan2}({}^R Y_T, {}^R X_T) & \text{if } ({}^R X_T, {}^R Y_T) \neq (0, 0), \\ 0 & \text{otherwise.} \end{cases} \quad (5)$$

In our work, we also consider the following hypothesis, which will be used in the stability proofs of Sect. IV-E.

Hypothesis 1. *The velocity of the target is negligible with respect to that of the robot.*

Under hypothesis 1:

$$\begin{cases} {}^R \dot{X}_T = -v_X + \omega {}^R Y_T \\ {}^R \dot{Y}_T = -v_Y - \omega {}^R X_T \\ {}^R \dot{\theta}_T = -\omega \end{cases} \quad (6)$$

Although this hypothesis is needed for the stability proof, in the experiments we have also validated our framework in cases where the target velocity is close to the robot one.

C. Obstacle occupation times

For obstacle modeling, we use the occupancy grid shown in Fig. 1: it is linked to $\mathcal{F}_{\mathcal{R}}$, with cell sides parallel to X_R and Y_R . Its longitudinal and lateral extensions are limited ($X_m \leq X_R \leq X_M$ and $Y_m \leq Y_R \leq Y_M$), to ignore obstacles that are too far to jeopardize the robot. Any grid cell \mathbf{c} centered at (X, Y) is considered occupied if an obstacle has been sensed in \mathbf{c} .

The set of occupied cells with their estimated velocities, is denoted by state vector \mathcal{O} :

$$\mathcal{O} = \{\mathbf{c}_1, \dots, \mathbf{c}_n, \dot{\mathbf{c}}_1, \dots, \dot{\mathbf{c}}_n\}. \quad (7)$$

This is used, along with the robot geometric and kinematic characteristics, to derive possible future collisions. Indeed, the estimations of the obstacles positions and velocities are updated at every iteration, by the Kalman observer designed in [15]. Then, for each \mathbf{c}_i that may be occupied by an obstacle within time horizon T_h , we can predict initial $t_{i0}(\mathcal{O}) \in [0, T_h]$ and final $t_{if}(\mathcal{O}) \in [t_{i0}, T_h]$ *obstacle occupation times*, in function of the set of occupied cell states \mathcal{O} .

III. OMNIDIRECTIONAL TENTACLES

We hereby present a generalization of the tentacles-based approach proposed in [13], to omnidirectional robots.

A. Definitions

We use a set of drivable paths (tentacles) both for perception and motion execution. Each tentacle j is a semicircle that starts in R and is tangent to the robot linear velocity. The norm of this velocity is: $\|v\| = \sqrt{v_X^2 + v_Y^2}$.

In contrast with the tentacles originally proposed in [15], our omnidirectional tentacles are characterized not only by their curvature (i.e., inverse radius)

$$\kappa_j = \begin{cases} \omega / \|v\| & \text{if } \|v\| \neq 0, \\ 0 & \text{otherwise,} \end{cases} \quad (8)$$

but also by their course angle

$$\alpha_j = \begin{cases} \text{atan2}(v_Y, v_X) & \text{if } \|v\| \neq 0, \\ 0 & \text{otherwise.} \end{cases} \quad (9)$$

In fact, note that on traditional nonholonomic systems, since the robot linear velocity is aligned with the robot heading $v_Y = 0$, thus $\alpha_j = 0$ for all control inputs (i.e., all tentacles are tangent to the robot heading).

Curvature κ_j belongs to \mathcal{K} , a uniformly sampled set¹:

$$\kappa_j \in \mathcal{K} = \{-\kappa_M, \dots, 0, \dots, \kappa_M\} \quad (10)$$

and α_j belongs to \mathcal{A} , another uniformly sampled set:

$$\alpha_j \in \mathcal{A} = \{\alpha_{Min}, \dots, 0, \dots, \alpha_{Max}\} \subseteq [-\pi, \pi[. \quad (11)$$

The set of tentacles is $\mathcal{T} = \mathcal{K} \times \mathcal{A}$. The total number of tentacles in \mathcal{T} is the product of the number of candidate curvatures by the number of candidate course angles. An example with 36 tentacles (3 curvatures \times 12 course angles)

¹For algorithmic reasons, we bound the tentacle curvature to an arbitrarily large value κ_M , although omnidirectional robots can follow tentacles of infinite curvature (i.e., pivot in place) whenever $\|v\| = 0$.

is shown in Fig. 1. Since tentacles are used both for perception and motion execution, a compromise between computational cost and control accuracy must be reached to set the sizes of \mathcal{H} and \mathcal{A} .

Each tentacle j is characterized by two classification areas (*collision* and *dangerous*), which are obtained by rigidly displacing, along the tentacle, two rectangular boxes, with increasing size. The boxes are overestimated with respect to the real robot dimensions. For each tentacle j , the sets of cells belonging to the two classification areas are noted \mathcal{C}_j and \mathcal{D}_j^2 . The sets \mathcal{O} , \mathcal{C}_j and \mathcal{D}_j are used to calculate the variables required in our control law, as will be explained just below. In particular, the largest classification area \mathcal{D}_j is used to select the safest tentacle and to assess its danger, while the thinnest one \mathcal{C}_j determines the - eventually needed - deceleration.

B. Robot occupation times

For each dangerous collision cell in tentacle j (i.e., for each cell $\mathbf{c}_i \in \mathcal{D}_j$), we compute the *robot occupation time* t_{ij} . This is an estimate of the time at which the box will enter the cell, assuming the robot follows the tentacle at the current velocity. To calculate $t_{ij}(\mathbf{c}_i, \mathbf{v}, \alpha_j, \kappa_j)$, we assume that the robot motion is uniform, and displace the box at the current robot velocities:

$$\begin{cases} v_X = \|\mathbf{v}\| \cos \alpha_j \\ v_Y = \|\mathbf{v}\| \sin \alpha_j \\ \omega_j = \kappa_j \|\mathbf{v}\|, \end{cases} \quad (12)$$

until the instant t_{ij} at which the box intersects cell \mathbf{c}_i .

C. Dangerous instants and collision instants

Once the obstacle and robot occupation times have been calculated for each cell, we can derive the earliest time instant at which a collision between obstacle and robot may occur on each tentacle j . By either checking all cells in \mathcal{D}_j , or focusing just on $\mathcal{C}_j \subset \mathcal{D}_j$, and using variables t_{i0} and t_{if} introduced in Sect. II-C, we discern between *dangerous instants* and *collision instants*. These are defined respectively as:

$$t_j = \inf_{\mathbf{c}_i \in \mathcal{D}_j} \{t_{ij} : t_{i0} \leq t_{ij} \leq t_{if}\}, \quad (13)$$

and

$$t_j^c = \inf_{\mathbf{c}_i \in \mathcal{C}_j} \{t_{ij} : t_{i0} \leq t_{ij} \leq t_{if}\}. \quad (14)$$

In both cases, we seek the earliest time at which a cell is simultaneously occupied by the obstacle and by the robot box. Assuming constant robot and obstacle velocities, these metrics give a good approximation of the time that the robot can travel along the tentacle without colliding. Further details are given in [13].

²For further details on the derivation of \mathcal{C}_j and \mathcal{D}_j , refer to [13].

IV. CONTROL SCHEME

A. Tentacle risk function

To assess the danger of each tentacle j , we design a *tentacle risk function*, by using t_j and tuned thresholds $t_d > 0$ and $t_s > t_d$ (d stands for dangerous, and s for safe):

$$H_j = \begin{cases} 0 & \text{if } t_j \geq t_s \\ \frac{1}{2} \left[1 + \tanh \left(\frac{1}{t_j - t_d} + \frac{1}{t_j - t_s} \right) \right] & \text{if } t_d < t_j < t_s \\ 1 & \text{if } t_j \leq t_d. \end{cases} \quad (15)$$

Note that H_j smoothly varies from 0, when possible collisions are in the far future, to 1, when they are forthcoming. If $H_j = 0$, the tentacle is tagged as *clear*.

To determine the best behaviour (among visual target tracking and obstacle avoidance) to adopt, we assess the danger of the environment via the risk function $H = H_v$ of the *visual task tentacle*, (κ_v, α_v) . This is the tentacle that best approximates the visual path that the robot would follow to reach the target in absence of obstacles. Depending on the value of H (noted *situation risk function*), we distinguish the contexts (*safe* or *unsafe*) explained below. The derivation of the visual task tentacle is also explained hereby.

B. Safe context

In the *safe context* ($H = 0$), no dangerous obstacle is detected on the robot path. In this case, it is desirable that the robot realizes the task of driving ${}^R\mathbf{p}_T$ to ${}^R\mathbf{p}_T^*$, while keeping as much as possible T within its field of view.

Since the angular velocity ω determines both the convergence of ${}^R\theta_T$ to ${}^R\theta_T^*$ (for pose regulation) and that of α_T to 0 (for target visibility), a compromise must be reached. We weigh the two objectives respectively with a gain $\lambda_\omega \in [0, 1]$ and with its complementary $1 - \lambda_\omega$. Priority is given to target visibility when the desired position is farther than ρ_α , and to pose regulation when it is nearer than ρ_θ^3 . In between, we use a smoothing function, as in (15):

$$\lambda_\omega(\rho^*) = \begin{cases} 1 & \text{if } \rho^* \geq \rho_\alpha \\ \frac{1}{2} \left[1 + \tanh \left(\frac{1}{\rho_\theta - \rho^*} + \frac{1}{\rho_\alpha - \rho^*} \right) \right] & \text{if } \rho_\theta < \rho^* < \rho_\alpha \\ 0 & \text{if } \rho^* \leq \rho_\theta. \end{cases} \quad (16)$$

The norm of the translation velocity v must be reduced, as the target is approached. We specify this through variable:

$$v_s(\rho^*) = \begin{cases} V & \text{if } \rho^* > \rho_v, \\ \frac{\rho^*}{\rho_v} V & \text{otherwise,} \end{cases} \quad (17)$$

with $V > 0$ the maximum desired value for v_s and $\rho_v > 0$ the distance at which the robot should slow down. Both V and ρ_v are easily tunable variables.

Finally, the translation velocity must be aligned with the heading towards the desired position α^* , when the target is far ($\lambda_\omega = 1$). As the target gets near ($\lambda_\omega < 1$), we also compensate the effects of the angular velocity ω in (6). In summary, the robot control inputs in the safe context are:

$$\begin{cases} v_X = v_s \cos \alpha^* + (1 - \lambda_\omega) \omega {}^R Y_T \\ v_Y = v_s \sin \alpha^* - (1 - \lambda_\omega) \omega {}^R X_T \\ \omega = \lambda_\omega \alpha_T + (1 - \lambda_\omega) ({}^R \theta_T - {}^R \theta_T^*). \end{cases} \quad (18)$$

³Both ρ_α and ρ_θ are pre-tuned, and $0 < \rho_\theta < \rho_\alpha$.

The above *safe context* control law (18) is also used to define the *visual path curvature* κ_s and *course angle* α_s :

$$\begin{cases} \kappa_s = [\lambda_\omega \alpha_T + (1 - \lambda_\omega) ({}^R\theta_T - {}^R\theta_T^*)] / \|v\| \\ \alpha_s = \text{atan2}(v_Y, v_X). \end{cases} \quad (19)$$

Note that in general κ_s and α_s will not correspond to a tentacle belonging to set \mathcal{T} , but they will be used to find the nearest tentacle in \mathcal{T} , i.e., the *visual task tentacle* (κ_v, α_v) that characterizes the *situation risk function* $H = H_v$, as explained in Sect. V-C.

C. Unsafe context

In the *unsafe context* ($H = 1$), dangerous obstacles are detected. The robot should circumnavigate them by following the best tentacle. The norm of the translation velocity must be reduced for safety reasons (i.e., to avoid collisions). We specify this by using a function $v_u \in [0, v_s]$:

$$\|v\| = v_u = \begin{cases} v_s & \text{if } t_b^c \geq t_s^c \\ v_s \sqrt{t_b^c - t_d^c / t_s^c - t_d^c} & \text{if } t_d^c < t_b^c < t_s^c \\ 0 & \text{if } t_b^c \leq t_d^c \end{cases} \quad (20)$$

(with $t_d^c > 0$ and $t_s^c > t_d^c$ two thresholds corresponding to dangerous and safe collision times) to guarantee that the vehicle decelerates (and eventually stops) as the collision instant on the best tentacle t_b^c decreases. Then, the robot control inputs in the unsafe context are:

$$\begin{cases} v_X = v_u \cos \alpha_b \\ v_Y = v_u \sin \alpha_b \\ \omega = \kappa_b v_u. \end{cases} \quad (21)$$

D. General control law

In *intermediate contexts* ($0 < H < 1$), the robot should navigate between the visual path, and the best tentacle. The transition between these two extremes will be driven by H . Using all the variables defined above, we can write our controller for visual navigation with obstacle avoidance:

$$\begin{cases} v_X = (1 - H) (v_s \cos \alpha^* + (1 - \lambda_\omega) \omega {}^R Y_T) + H v_u \cos \alpha_b \\ v_Y = (1 - H) (v_s \sin \alpha^* - (1 - \lambda_\omega) \omega {}^R X_T) + H v_u \sin \alpha_b \\ \omega = (1 - H) (\lambda_\omega \alpha_T + (1 - \lambda_\omega) ({}^R\theta_T - {}^R\theta_T^*)) + H v_u \kappa_b. \end{cases} \quad (22)$$

Note that for $H = 0$ this coincides with (18), and for $H = 1$, with (21).

E. Stability Analysis

Let us now focus on some interesting stability properties of control law (22).

Property 1. *In the safe context, if $\rho^* \geq \rho_\alpha$ (and therefore $\lambda_\omega = 1$) controller (22) guarantees asymptotic convergence of task vector $s = [\rho^* \alpha_T]^\top$ to $s^* = [\rho_\alpha 0]^\top$. Therefore, the robot will orient its heading towards the target while simultaneously approaching it until $\rho^* = \rho_\alpha$.*

Proof. First, let us derive α_T with respect to time, using (5) (for $\rho_T \neq 0$), along with (6):

$$\dot{\alpha}_T = \frac{v_X {}^R Y_T - v_Y {}^R X_T}{\rho_T^2} - \omega. \quad (23)$$

Injecting the safe context controller (18) in (23) when $\lambda_\omega = 1$:

$$\dot{\alpha}_T = \frac{v_s}{\rho_T^2} ({}^R Y_T \cos \alpha^* - {}^R X_T \sin \alpha^*) - \alpha_T. \quad (24)$$

Since ${}^R Y_T / \rho_T = \sin \alpha_T$ and ${}^R X_T / \rho_T = \cos \alpha_T$:

$$\dot{\alpha}_T = \frac{v_s}{\rho_T} \sin(\alpha_T - \alpha^*) - \alpha_T. \quad (25)$$

Note that when $\rho^* \geq \rho_\alpha$, $\alpha_T \approx \alpha^*$, since the Euclidean distance between points R and T^* becomes neglectable with respect to ρ^* (see Fig.2). Hence, (25) becomes:

$$\dot{\alpha}_T = -\alpha_T. \quad (26)$$

Now, let us derive ρ^* with respect to time, using (4):

$$\dot{\rho}^* = \frac{({}^R X_T - {}^R X_T^*)^R \dot{X}_T + ({}^R Y_T - {}^R Y_T^*)^R \dot{Y}_T}{\rho^*}. \quad (27)$$

From (3) if $\rho^* \neq 0$ (as is the case here):

$$\begin{cases} {}^R X_T - {}^R X_T^* = \rho^* \cos \alpha^* \\ {}^R Y_T - {}^R Y_T^* = \rho^* \sin \alpha^*. \end{cases} \quad (28)$$

Injecting this in (27) yields:

$$\dot{\rho}^* = -(v_X \cos \alpha^* + v_Y \sin \alpha^*) + \omega \rho_T \sin(\alpha_T - \alpha^*), \quad (29)$$

and with the safe context controller (18) since $\alpha_T \approx \alpha^*$:

$$\dot{\rho}^* = -v_s. \quad (30)$$

Finally, let us consider the Lyapounov function $\mathcal{V} = \mathbf{e}^\top \mathbf{e} / 2$ where $\mathbf{e} = \mathbf{s} - \mathbf{s}^*$. Its time derivative is:

$$\dot{\mathcal{V}} = \dot{\mathbf{e}}^\top \mathbf{e} = [\dot{\rho}^* \dot{\alpha}_T] \begin{bmatrix} \rho^* - \rho_\alpha \\ \alpha_T \end{bmatrix}. \quad (31)$$

Injecting (26) and (30) in (31) yields:

$$\dot{\mathcal{V}} = -v_s (\rho^* - \rho_\alpha) - \alpha_T^2, \quad (32)$$

which is clearly negative definite for $\mathbf{e} \neq 0$ when $\rho^* \geq \rho_\alpha$. \square

An alternative control strategy would have consisted in applying the linear velocity that cancels the effect of ω in (6):

$$\begin{cases} v_X = v_s \cos \alpha^* + \omega {}^R Y_T \\ v_Y = v_s \sin \alpha^* - \omega {}^R X_T. \end{cases} \quad (33)$$

Although this controller guarantees asymptotic convergence of both $\omega {}^R X_T$ and $\omega {}^R Y_T$ to 0, it makes the value of α_T constant throughout navigation. Indeed, plugging (33) in (23) yields:

$$\dot{\alpha}_T = \frac{v_s}{\rho} \sin(\alpha_T - \alpha^*), \quad (34)$$

which is neglectable, since $\alpha_T \approx \alpha^*$. In summary, controller (33) does not give the possibility of centering the target in the field of view, as one would expect (particularly for far target).

Property 2. *In the safe context, if $\rho^* \leq \rho_\theta$, controller (22) guarantees asymptotic convergence of task vector $s = [\rho^* {}^R\theta_T]^\top$ to $s^* = [0 {}^R\theta_T^*]^\top$. Hence, the robot will asymptotically converge to the desired pose with respect to the target.*

Proof. When $\lambda_\omega = 0$ (since $\rho^* \leq \rho_\theta$), injecting the safe context controller (18) in 29 yields:

$$\dot{\rho}^* = -v_s, \quad (35)$$

and from the last equation of (6):

$${}^R\dot{\theta}_t = {}^R\theta_t^* - {}^R\theta_t. \quad (36)$$

Consider the same Lyapounov function as above. Since ${}^R\mathbf{p}_T^*$ is constant, the Lyapounov function derivative is:

$$\dot{\mathcal{V}} = \dot{\mathbf{e}}^\top \mathbf{e} = [\dot{\rho}^* {}^R\dot{\theta}_t] \begin{bmatrix} \rho^* \\ {}^R\theta_t - {}^R\theta_t^* \end{bmatrix}. \quad (37)$$

If $\rho^* \neq 0$, injecting (35) and (36) in (37) yields:

$$\dot{\mathcal{V}} = -v_s \rho^* - ({}^R\theta_t - {}^R\theta_t^*)^2, \quad (38)$$

which is clearly negative definite for $\mathbf{e} \neq 0$.

If $\rho^* = 0$, ${}^R X_T = {}^R X_T^*$ and ${}^R Y_T = {}^R Y_T^*$. Hence, $\dot{\mathcal{V}} = -({}^R\theta_t - {}^R\theta_t^*)^2$, which is also negative definite for $\mathbf{e} \neq 0$. \square

Property 3. *In the unsafe context, if moving ($\|v\| \neq 0$), the robot will precisely follow the best tentacle (κ_b, α_b).*

Proof. When $H = 1$, controller (22) becomes (21), and it is trivial to see, by applying (8) and (9) that whenever $\|v\| \neq 0$, the curvature and course angle will respectively coincide with κ_b and α_b . \square

These three properties outline some nice features of our framework. For instance, consider the safe context. Property 1 shows that from far, the robot will orient its heading towards the target (hence maintain it within its field of view), while approaching it. When the robot is near enough to the target, Property 2 is triggered. Then, the robot will servo its heading towards the desired relative orientation, while converging to the desired position with respect to the target.

It is noteworthy to mention that the properties are valid in given operating situations (H and λ_ω either null or unitary). It is very difficult (and out of scope here) to study analytically the behaviour of the system in the intermediate situations, i.e., when H and λ_ω are different from 0 or 1. However, the smooth design of these two functions, as well the extensive experimental validation of (22) (see Sect. VII) make us very confident about the global performance of our framework.

In the next section, we explain the strategy that is adopted to select the best tentacle to be followed in the unsafe context.

V. TENTACLES SELECTION STRATEGY

In this section, we describe our strategy for selecting the best tentacle (κ_b, α_b), that allows the robot to avoid the obstacles while simultaneously performing the visual task. To this end, we must first define a metric for sorting the tentacles. This is explained in Sect. V-A. The visibility constraints to be satisfied by the best tentacle are then described in Sect. V-B. These criteria are finally used to select the best tentacle, as explained in Sect. V-C.

A. Sorting tentacles

To apply any search algorithm to set \mathcal{T} , in order to find the best tentacle (κ_b, α_b), the set must be somehow sorted. To this end, we must find a metric characterizing similarity (or difference) among tentacles. This is a non-trivial task, since \mathcal{T} is defined in a discrete non-Euclidean space:

$$\mathcal{T} = \mathcal{K} \times \mathcal{A} \subset \mathbb{R} \times \mathbb{SO}(2), \quad (39)$$

where a distance metric cannot be defined, without weighing – arbitrarily – the relative importance of a scalar (κ_j) with respect to an angle (α_j). To solve this problem, we rely on the following property.

Property 4. *Let an omnidirectional robot be modeled as a point. Its Cartesian position, after having followed tentacle (κ_j, α_j) at velocity $\|v\|$ for an iteration $\Delta t \ll 1$, depends only on the scalar function: $\phi_R = \alpha_j + \frac{\|v\| \Delta t}{2} \kappa_j$.*

Proof. Since we model the robot as a point, only changes in the robot position (not orientation) are considered. We start by calculating the robot position change after Δt , in function of (κ_j, α_j). To this end, we define a fixed frame $\mathcal{F}_\theta(O, X_O, Y_O)$ that corresponds to the robot frame at the beginning of the iteration (see Fig. 3). For each tentacle j , we can calculate the robot position ${}^O\mathbf{p}_R = [{}^OX_R \ {}^OY_R]^\top$ in \mathcal{F}_θ after the robot has followed the tentacle for time Δt . We can relate the derivative of the robot pose in \mathcal{F}_θ and the control inputs:

$$\begin{cases} {}^O\dot{X}_R = v_X \cos({}^O\theta_R) - v_Y \sin({}^O\theta_R) \\ {}^O\dot{Y}_R = v_X \sin({}^O\theta_R) + v_Y \cos({}^O\theta_R) \\ {}^O\dot{\theta}_R = \omega. \end{cases} \quad (40)$$

Using (12), we can rewrite (40) in function of the followed tentacle, i.e., in function of κ_j and α_j :

$$\begin{cases} {}^O\dot{X}_R = \|v\| (\cos \alpha_j \cos({}^O\theta_R) - \sin \alpha_j \sin({}^O\theta_R)) \\ {}^O\dot{Y}_R = \|v\| (\cos \alpha_j \sin({}^O\theta_R) + \sin \alpha_j \cos({}^O\theta_R)) \\ {}^O\dot{\theta}_R = \|v\| \kappa_j. \end{cases} \quad (41)$$

By integrating this expression, we can obtain the robot position at Δt . We distinguish two cases according to κ_j :

- if $\kappa_j = 0$ (i.e. the tentacle is a straight line), the robot position will be:

$$\begin{cases} {}^OX_R = \|v\| \Delta t \cos \alpha_j \\ {}^OY_R = \|v\| \Delta t \sin \alpha_j; \end{cases} \quad (42)$$

- if $\kappa_j \neq 0$, the robot position will be:

$$\begin{cases} {}^OX_R = 2/\kappa_j \sin(\kappa_j \|v\| \Delta t/2) \cos(\alpha_j + \kappa_j \|v\| \Delta t/2) \\ {}^OY_R = 2/\kappa_j \sin(\kappa_j \|v\| \Delta t/2) \sin(\alpha_j + \kappa_j \|v\| \Delta t/2). \end{cases} \quad (43)$$

Converting the position to polar coordinates (r_R, ϕ_R), with $r_R = \sqrt{{}^OX_R^2 + {}^OY_R^2}$ and $\phi_R = \text{atan2}({}^OY_R, {}^OX_R)$ (see Fig. 3) yields

$$r_R(\alpha_j, \kappa_j) = \begin{cases} \|v\| \Delta t & \text{if } \kappa_j = 0 \\ \frac{2}{\kappa_j} \sin\left(\frac{\kappa_j}{2} \|v\| \Delta t\right) & \text{otherwise,} \end{cases} \quad (44)$$

$$\phi_R(\alpha_j, \kappa_j) = \alpha_j + \frac{\|v\| \Delta t}{2} \kappa_j. \quad (45)$$

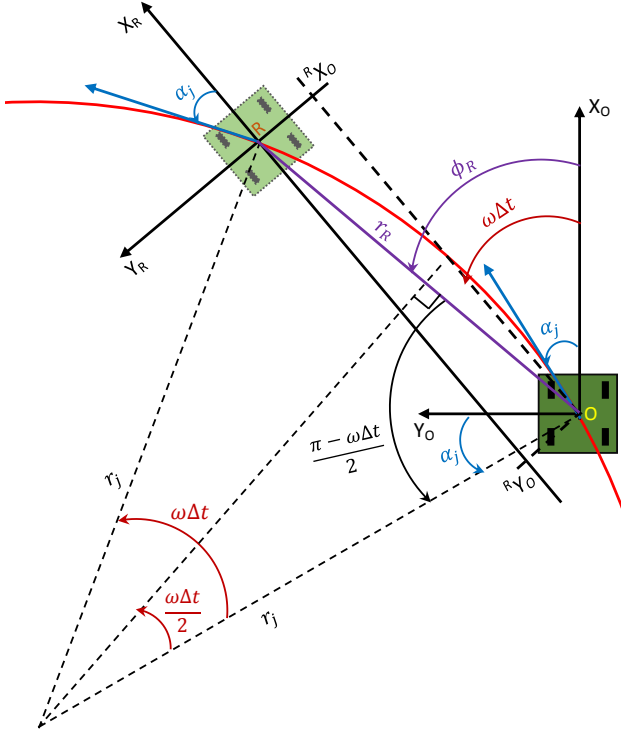


Fig. 3. Variables needed for tentacle selection.

Since the robot movement is small during an iteration (as $\Delta t \ll 1$), $\sin\left(\frac{\kappa_j}{2} \|v\| \Delta t\right) \approx \frac{\kappa_j}{2} \|v\| \Delta t$, and therefore r_R will not vary much from a tentacle to the other ($r_R \approx \|v\| \Delta t$). Hence, the robot position after having followed the tentacle at velocity $\|v\|$ for Δt will depend only on ϕ_R . \square

As a consequence of Property 4, we have decided to sort the tentacles according to their values of ϕ_R , calculated using (45), and noted $\phi_{R,j}$ for each tentacle j .

B. Tentacles guaranteeing visibility

In this section, we introduce the visibility constraints in our obstacles avoidance strategy. To ensure that the target is not lost during navigation, the best tentacle should keep the target in sight. However, this is not possible for all tentacles, since the robot is constrained to look in its heading direction. Here, we consider as tentacles that guarantee visibility, those that will maintain the target in the field of view after an iteration Δt .

For a given tentacle j , we define (again, refer to Fig. 3):

- 1) $(^O X_T, ^O Y_T, ^O \theta_T)$: the target pose (at $t = 0$) in the initial robot frame $\mathcal{F}_O(R_O, X_O, Y_O)$
- 2) $(^R X_T, ^R Y_T, ^R \theta_T)$: the target pose (at $t = \Delta t$) in the robot frame $\mathcal{F}_R(R_R, X_R, Y_R)$.

The relation between these two poses is given by :

$$\begin{bmatrix} ^R X_T \\ ^R Y_T \\ ^R \theta_T \\ 1 \end{bmatrix} = \begin{bmatrix} \cos(\omega \Delta t) & \sin(\omega \Delta t) & 0 & ^R X_O \\ -\sin(\omega \Delta t) & \cos(\omega \Delta t) & 0 & ^R Y_O \\ 0 & 0 & 1 & -\omega \Delta t \\ 0 & 0 & 0 & 1 \end{bmatrix} \begin{bmatrix} ^O X_T \\ ^O Y_T \\ ^O \theta_T \\ 1 \end{bmatrix} \quad (46)$$

where $(^R X_O, ^R Y_O)$ are the coordinates of the origin of \mathcal{F}_O in \mathcal{F}_R . Typically, after Δt these can be expressed in polar coordinates as:

$$\begin{cases} ^R X_O = -r_R \cos(\phi_R - \omega \Delta t) \\ ^R Y_O = -r_R \sin(\phi_R - \omega \Delta t) \end{cases} \quad (47)$$

Injecting (47) in (46) and using (45), we derive the target position $(^R X_T, ^R Y_T)$ in the robot frame after Δt . We distinguish two cases:

- when $\kappa_j \neq 0$:

$$\begin{cases} ^R X_T = \cos(\kappa_j \|v\| \Delta t) ^O X_T + \sin(\kappa_j \|v\| \Delta t) ^O Y_T \\ \quad - 2/\kappa_j \sin(\kappa_j \|v\| \Delta t/2) \cos(\alpha_j - \kappa_j \|v\| \Delta t/2) \\ ^R Y_T = -\sin(\kappa_j \|v\| \Delta t) ^O X_T + \cos(\kappa_j \|v\| \Delta t) ^O Y_T \\ \quad - 2/\kappa_j \sin(\kappa_j \|v\| \Delta t/2) \sin(\alpha_j - \kappa_j \|v\| \Delta t/2), \end{cases} \quad (48)$$

- if $\kappa_j = 0$:

$$\begin{cases} ^R X_T = ^O X_T - \|v\| \Delta t \cos(\alpha_j) \\ ^R Y_T = ^O Y_T - \|v\| \Delta t \sin(\alpha_j). \end{cases} \quad (49)$$

For the target to be visible, its position in the robot frame must satisfy the following constraints:

$$\begin{cases} ^R X_T > ^R X_C \\ ^R Y_C - (^R X_T - ^R X_C) \tan\left(\frac{\beta}{2}\right) < ^R Y_T < ^R Y_C + (^R X_T - ^R X_C) \tan\left(\frac{\beta}{2}\right), \end{cases} \quad (50)$$

with $(^R X_C, ^R Y_C)$ the sensor center coordinates in \mathcal{F}_R and β its field of view (see Fig. 1). In summary, to determine whether tentacle j guarantees target visibility, it is sufficient to inject its (κ_j, α_j) into (48) or (49) and then check if the resulting $^R X_T$ and $^R Y_T$ verify constraints (50).

C. Selecting the best tentacle

Let us describe the best tentacle selection strategy.

At *initialization*, all tentacles in set $\mathcal{T} = \mathcal{K} \times \mathcal{A}$ are sorted according to their $\phi_{R,j}$, calculated with (45).

Then, at *each iteration* Δt we proceed as follows (see Algorithm 1).

- 1) The subset of all tentacles that guarantee the visibility constraints is derived as explained in Sect. V-B. If the number of tentacles in this subset is sufficient (at least 5 in this work), all other tentacles are removed from \mathcal{T} . Otherwise, the entire set \mathcal{T} is kept, to privilege obstacle avoidance over occlusion avoidance. This choice is motivated on one hand by obvious safety reasons, and on the other by the possibility – offered by the method that will be explained in the next Section – of estimating the target pose even when it is not visible.
- 2) For the path that the robot would perform if there were no obstacles, i.e., if the safe context controller (18) was applied, we compute: the course angle α_s , curvature κ_s using (19), and polar angular coordinate $\phi_{R,s}$.
- 3) The tentacle that best approximates the visual path in \mathcal{T} (i.e., the nearest in terms of ϕ_R) is computed; we denote it as the *visual task tentacle* (κ_v, α_v) and calculate its situation risk function as H_v using (15). This is also the value that will be used in control law (22): $H = H_v$.

Algorithm 1 Selecting the best tentacle

input: Sorted set of tentacles \mathcal{T} , visual path (α_s, κ_s) , previous best tentacle (α_p, κ_p) , and target pose ${}^O\mathbf{p}_T$.

output: Risk function H and best tentacle (α_b, κ_b) (if $H \neq 0$).

```

1:  $N \leftarrow \text{FindVisibilityGuaranteeingTentacles}(\mathcal{T}, {}^O\mathbf{p}_T)$ ;
2: if  $N > 5$  then
3:    $\mathcal{T} \leftarrow \text{RemoveOtherTentacles}(\mathcal{T})$ ;
4: end if
5:  $\phi_{R,s} \leftarrow \text{CalculateSortingAngle}(\alpha_s, \kappa_s)$ ;
6:  $\phi_{R,v} \leftarrow \text{FindNearestSortingAngle}(\mathcal{T}, \phi_{R,s})$ ;
7:  $(\alpha_v, \kappa_v) \leftarrow \text{CalculateTentacleParameters}(\phi_{R,v})$ ;
8:  $H \leftarrow \text{CalculateRiskFunction}(\alpha_v, \kappa_v)$ ;
9:  $(\alpha_b, \kappa_b) \leftarrow \text{null}$ ;
10: if  $H \neq 0$  then
11:    $\phi_{R,p} \leftarrow \text{CalculateSortingAngle}(\alpha_p, \kappa_p)$ ;
12:   if  $\phi_{R,v} < \phi_{R,p}$  then
13:      $(\phi_i, \phi_f) \leftarrow (\phi_{R,v}, \phi_{R,p})$ ;
14:   else
15:      $(\phi_i, \phi_f) \leftarrow (\phi_{R,p}, \phi_{R,v})$ ;
16:   end if
17:    $(\alpha_b, \kappa_b) \leftarrow \text{FindNearestClearTentacle}(\mathcal{T}, [\phi_i, \phi_f])$ ;
18:   if  $(\alpha_b, \kappa_b) = \text{null}$  then
19:      $(\alpha_b, \kappa_b) \leftarrow \text{FindNearestClearTentacle}(\mathcal{T},$ 
20:        $[\phi_{min}, \phi_i \cup \phi_f, \phi_{max}])$ ;
21:   end if
22: end if
23: return  $(H, (\alpha_b, \kappa_b))$ ;

```

- 4) If $H = 0$, the visual task tentacle is clear and the safe context controller (18) can be applied.
- 5) Instead, if $H \neq 0$, we seek a clear tentacle (i.e., one with $H_j = 0$).
 - a) First, we search among the tentacles with $\phi_{R,j}$ between the one of the visual task tentacle and that of the best tentacle at the previous iteration.
 - b) If many clear tentacles are present, the nearest to the visual task tentacle is chosen.
 - c) If none of them is clear, we search among the others (the tentacles that are not between the visual task and the previous best tentacles). Again, the best tentacle will be the clear one that is closest to the visual task tentacle.

VI. TARGET DETECTION AND TRACKING

In this section, we describe our approach for detecting and tracking over time the target pose (position and orientation) in the robot frame, ${}^R\mathbf{p}_T$. This is done by the robot visual sensor/s with an image processing algorithm described in Sect. VI-A. If the target is not visible, because it exits the field of view or is occluded, an alternative method is applied, as explained in Sect. VI-B.

A. Vision-based target detection

Our target detection algorithm relies on the following assumptions:

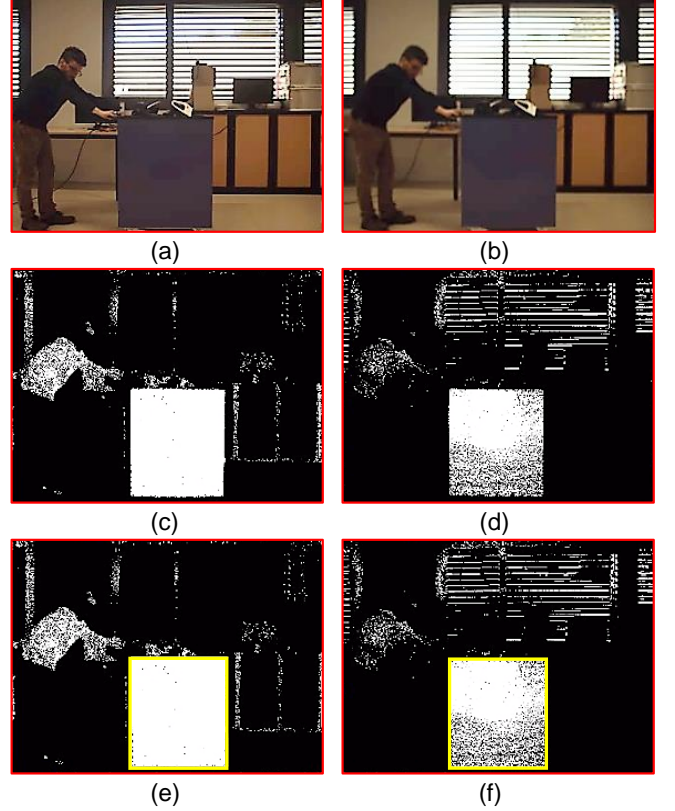


Fig. 4. Target detection and tracking in the left and right images. (a-b) Raw images. (c-d) Blob detection. (e-f) Cart contour extraction.

- the target is characterized by a predominant color,
- the visible part of the target is planar,
- as position of the target $({}^RX_T, {}^RY_T)$, we take the Cartesian coordinates of the visible plane in \mathcal{F}_R ,
- as target orientation ${}^R\theta_T$, we take the angular offset from X_R to the normal vector entering the visible plane.

The described algorithm has been developed for the sensor suite available on our self-made robotic platform BAZAR [32]. This is composed of a forward looking fixed pair of 55.8° field of view cameras operating at 30 Hz, and two 270° Hokuyo lidars placed at opposite corners of the base, and operating at 40 Hz. The algorithm relies on both cameras, and on the forward looking lidar. The lidar however, is used only when the target is near, to obtain a precise estimation of ${}^R\mathbf{p}_T$. The reason is that, although lidar measurements are more precise on a short range, they are biased by inaccuracy and false positives on the long range. On the other hand, from far, when only vision is used, orientation ${}^R\theta_T$ cannot be properly estimated. Note that controller (22) does not require ${}^R\theta_T$ as long as $\rho^* \geq \rho_\alpha$. Hence, the most intuitive design choice is to start using the lidar only when $\rho^* < \rho_\alpha$. While $\rho^* \geq \rho_\alpha$, only the target position $({}^RX_T, {}^RY_T)$ is calculated from vision without using lidar data. Even if this estimation is imprecise, it will make the robot approach the target, while orienting its heading towards it until, for $\rho^* < \rho_\alpha$, the lidar will be activated and ${}^R\theta_T$ will also be estimated, to drive the robot to the desired pose with

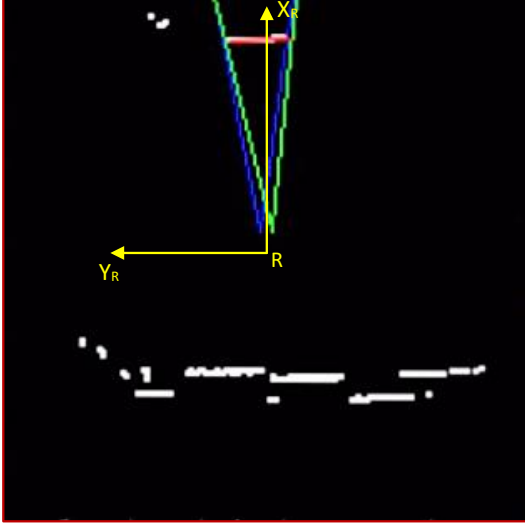


Fig. 5. Detecting the cart face segment using lidar measurements.

respect to the target.

For image processing, the same steps (developed with OpenCV⁴) are applied to the left and right cameras. These steps are detailed below and illustrated in Fig. 4.

- 1) The images are binarized with a logic conjunction (*and* operator) of predefined ranges in the Hue, Saturation and Value color space. This way, pixels of a certain color (blue in Figures 4c and 4d) can be isolated.
- 2) A dilation and an erosion are applied to the binary image to form blobs of pixels of the target's color.
- 3) The blob with the largest contour is extracted (Figures 4e and 4f).
- 4) Using the knowledge of the real target height (in meters) along with the camera intrinsic and extrinsic parameters, the position of the front face centroid is projected in \mathcal{F}_R to obtain $(^R X_T, ^R Y_T)$.
- 5) If the blob is detected by both cameras, the average of the two positions is used.

As the robot approaches the target and $\rho^* < \rho_\alpha$, the front lidar is also utilized, to improve the position, and add the orientation estimates. We proceed as follows (see Fig. 5):

- 1) A high resolution occupancy grid (cell size 3×3 cm) is built from lidar measurements.
- 2) The two side borders of the blob are projected in the grid for both the left (blue cone in Fig. 5) and right (green) cameras.
- 3) The Hough transform is applied to detect all line segments in the two cones.
- 4) The extreme (nearer and farther) corners among all these line segments are used to define a region of interest, where linear regression on the raw lidar data is used to find the visible target projection (red segment in Fig. 5).
- 5) From this segment, the target pose $^R \mathbf{p}_T$ is derived.
- 6) A Kalman Filter (with state vector composed of $^R \mathbf{p}_T$ and $^R \dot{\mathbf{p}}_T$) is finally used to ensure continuity and robustness

of the target pose estimation.

B. Dealing with total loss of the target

If none of the tentacles that guarantee robot safety can satisfy the visibility constraints, the target will exit the field of view and the above approach cannot be applied. The same applies if obstacles on the robot path provoke a partial or total target occlusion.

To overcome both problems, we estimate the target pose $(^R X_T, ^R Y_T, ^R \theta_T)$ in the robot frame by using its previous pose $(^O X_T, ^O Y_T, ^O \theta_T)$ and control inputs (v_X, v_Y, ω) . This is done by integrating the target pose over time interval Δt , using (46) and (47):

- if $\omega \neq 0$:

$$\begin{cases} ^R X_T = \cos(\omega \Delta t) ^O X_T + \sin(\omega \Delta t) ^O Y_T \\ \quad - 2v/\omega \sin(\omega \Delta t/2) \cos(\alpha - \omega \Delta t/2) \\ ^R Y_T = -\sin(\omega \Delta t) ^O X_T + \cos(\omega \Delta t) ^O Y_T \\ \quad - 2v/\omega \sin(\omega \Delta t/2) \sin(\alpha - \omega \Delta t/2) \\ ^R \theta_T = ^O \theta_T - \omega \Delta t, \end{cases} \quad (51)$$

with α defined as in (9), but in the general case (not just $\alpha \in \mathcal{A}$).

- If $\omega = 0$, the previous expression becomes:

$$\begin{cases} ^R X_T = ^O X_T - v_X \Delta t \\ ^R Y_T = ^O Y_T - v_Y \Delta t \\ ^R \theta_T = ^O \theta_T. \end{cases} \quad (52)$$

Injecting these equations in the same Kalman Filter as above (with state vector composed of $^R \mathbf{p}_T$ and $^R \dot{\mathbf{p}}_T$), it is possible to deal with the target total loss, by predicting its location without affecting the robot behaviour. In practice, we use either (51) or (52) (depending on ω) in control law (22).

VII. EXPERIMENTAL VALIDATION

Here, we report the simulated and real experiments that we performed to validate our approach. These are also shown in the video attached to this paper⁵. In all tests, we use the same setup and parameters, the only difference being the wheeled platform: KUKA youBot in simulations and Neobotix MPO700 (the base of our BAZAR platform) in real experiments. The target is a blue wheeled cart, similar to the one used for kitting in automotive manufacturing by our partner PSA Peugeot Citroën. It is automatically moved in simulations, and manually pushed in the real experiments. For simplicity, we position the target in the robot field of view at the beginning of each simulation/experiment. A “target searching” navigation procedure, out of scope here, could be devised as future work.

Both the simulated KUKA youBot and real Neobotix MPO700 are equipped with the BAZAR sensor suite described in Sect. VI-A. In the visibility constraint equation (50), we use as C the midpoint of the 2 optical centers and as β (conservatively) the field of view of the cameras (55.8°). We set to $\Delta t = 200$ ms the sampling time of our algorithm, that includes visual processing (Sect. VI), tentacle processing

⁴ <http://opencv.org/>

⁵ Also visible online at <https://youtu.be/K9yoNlqkqSI>

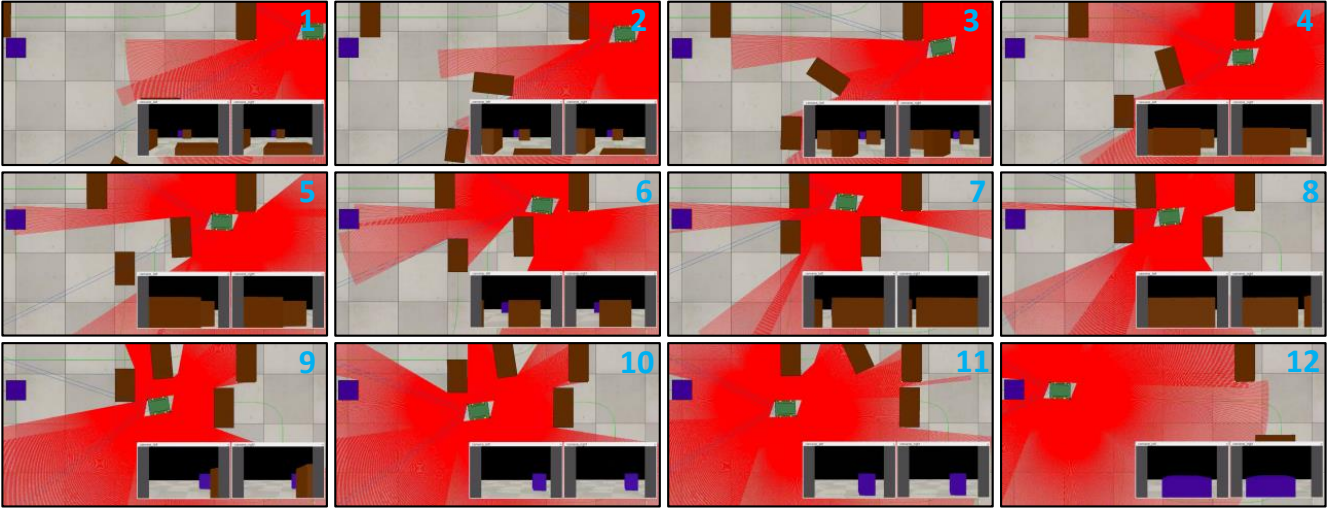


Fig. 6. V-REP Scenario A: the robot (green box), equipped with two cameras (blue cones) and lidar scanners (red lines) navigates towards a static target (blue) while avoiding collisions and dealing with occlusions caused by one static and three moving obstacles (all brown).

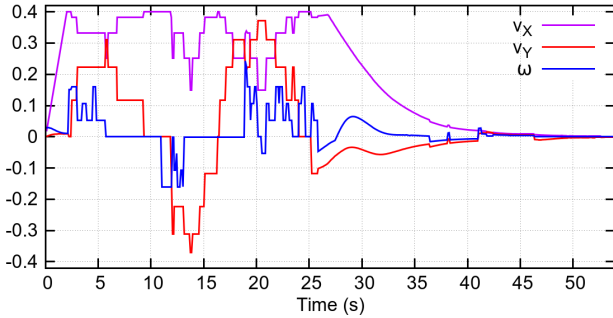


Fig. 7. V-REP Scenario A: robot control inputs (linear velocities v_x and v_y in m/s and angular velocity ω in rad/s) during the simulation.

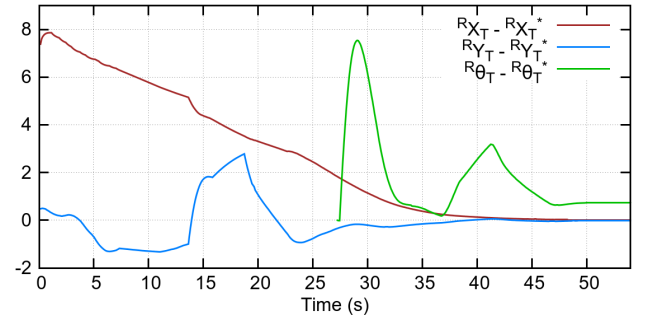


Fig. 8. V-REP Scenario A: evolution of position (in meters) and orientation (in degrees) errors of the target in the robot frame.

(Sections III and V) and control (Sect. IV) in a unique thread. This choice of Δt is motivated by the limitations of the PC graphics card; in the future, we plan on parallelizing the computation on multiple threads, to reduce Δt . The obstacle detecting occupancy grid (with $X_M = Y_M = 3$ m, $X_m = Y_m = -3$ m, and cell size 10×10 cm) is built by projecting the lidar readings from the two lidars. We use 147 tentacles (7 curvatures \times 21 course angles), with $\kappa_M = 0.4 \text{ m}^{-1}$, $\alpha_{Min} = -170^\circ$, and $\alpha_{Max} = 170^\circ$. The maximum translational velocity, that is applied in the safe environment, and far from the target using (17) is $V = 0.4 \text{ ms}^{-1}$. For the situation risk function we use $t_s = 3.5$ s and $t_d = 3$ s, for the unsafe translational velocity $t_s^c = 2.25$ s and $t_d^c = 1.5$ s, and for the visual task $\rho_\alpha = 3.5$ m $\rho_\theta = 1$ m and $\rho_v = 2$ m.

A. Simulations

Let us recall that the main goal is to perform vision-based omnidirectional navigation in the presence of static or moving – and possibly occluding – obstacles. To this end, preliminary simulations were carried out in V-REP⁶, with the KUKA youBot, an omnidirectional mobile robot with 4

Swedish wheels. In V-REP, we have designed three scenarios A, B, and C shown respectively in Fig. 6, Fig. 9, and Fig. 10, along with the images acquired by the robot cameras during the simulations. In these figures, the robot, target and obstacles are represented respectively by green, blue and brown boxes. In scenario A, the visual target is static, whereas in scenarios B and C, it is moving. In all scenarios, the robot is able to perform the visual task and to reach the desired relative pose ${}^R\mathbf{p}_T^*$, while avoiding collisions and managing occlusions provoked by the obstacles. We hereby describe the robot behaviour for each scenario.

1) *Scenario A*: The environment is cluttered, with four obstacles that may partially or totally occlude the target (see Fig. 6). The closest obstacle is static, while the three others move. We have plotted, in Fig. 7, the robot control inputs during this navigation task. The plot shows that after approximately 2 s, the robot is deviated (v_y) and oriented (ω) so that the camera is pointing at the target. When the robot is near the first obstacle (at $t \approx 3$ s), it starts avoiding it while keeping the target in the camera field of view. The target is partially occluded by another obstacle without affecting the robot behaviour. Then, the robot progresses toward the desired pose before avoiding the second obstacle which induces a total

⁶<http://www.coppeliarobotics.com>

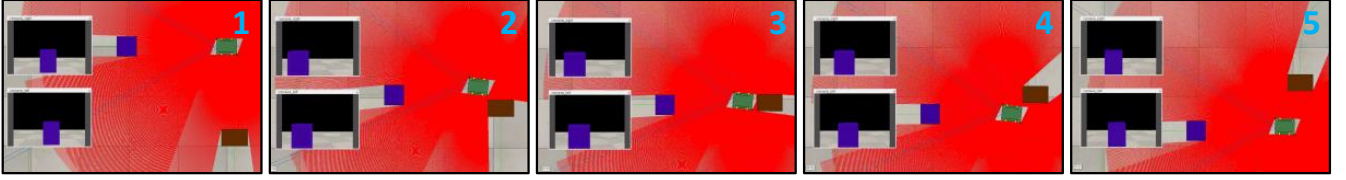


Fig. 9. V-REP Scenario B: the robot performs lateral avoidance of a moving obstacle while maintaining visibility of a moving target.

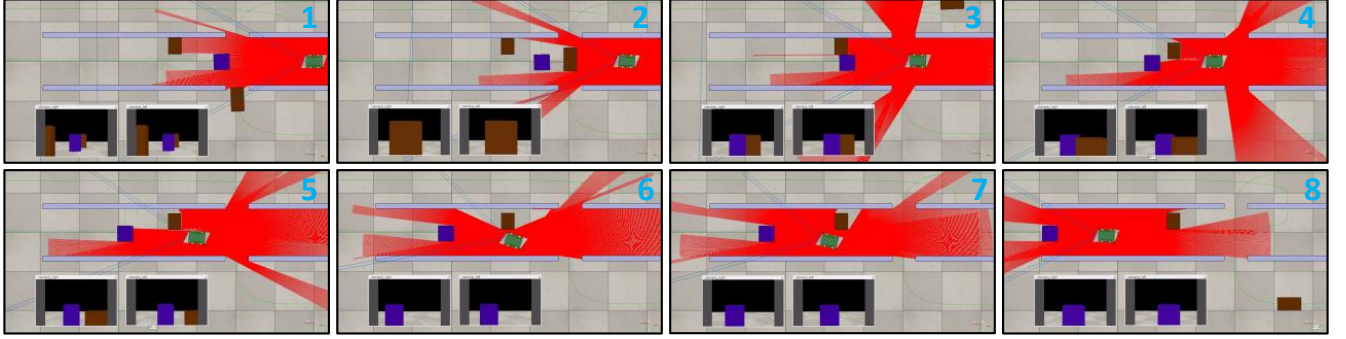


Fig. 10. V-REP Scenario C: the robot follows a moving target in a cluttered corridor with two obstacles (one moving, one static).

occlusion of the target. Nevertheless, the robot performs its task thanks to the target pose estimation module described in Sect. VI-B. Afterwards, the robot succeeds in avoiding the last two obstacles and reaches the target despite the occlusions they cause (see images 7 and 8 in Fig. 6). Then (at $t \approx 33$ s), the environment is free again, and the visual task can be performed for the rest of the experiment. At the end, the robot decelerates and stops when the desired pose relative to the target has been reached. The target position error (${}^R X_T - {}^R X_T^*, {}^R Y_T - {}^R Y_T^*$) and orientation error (${}^R \theta_T - {}^R \theta_T^*$) are plotted in Fig. 8. Notice that the target orientation ${}^R \theta_T$ is not estimated until $t \approx 27$ s since before that, $\rho^* \geq \rho_\alpha$, as explained in Sect. VI-A. As we can see in these plots, all the errors converge to zero while the robot is driving to the target. This result is coherent, as the visual task consists in moving the target from the initial to the desired pose in \mathcal{F}_R .

2) *Scenario B*: This scenario (shown in Fig. 9) is designed to test lateral collision avoidance by exploiting the omnidirectional characteristic of the robot. The target is moving in the lateral direction with regards to the robot (roughly in the direction parallel to the Y_R axis) and an obstacle approaches the robot in the same direction, but opposite verse. After reaching the desired pose relative to the moving target, the controller deviates the robot to maintain its relative heading (hence to guarantee target visibility) while avoiding the moving obstacle. When the environment is clear again, the robot returns to the desired relative pose.

3) *Scenario C*: Here, we consider navigation in a corridor (light purple in Fig. 10), common in indoor environments. The target is moving in the corridor, and the robot must follow it, while avoiding the walls as well as two brown boxes. The first one moves perpendicularly to the path and induces an occlusion, while the second one is static and presents a risk of collision. Despite the limited mobility within this environment, the robot is capable of dealing with the occlusion and avoiding

both obstacles, while successfully following the target.

B. Real experiments

After the simulations, we have validated our approach in extensive real experiments, carried out on our Neobotix MPO700 platform. This is an omnidirectional robot with 4 steerable wheels, hence with a reduced mobility as compared to the Swedish wheels platform used in V-REP. The MPO700 wheels are driven by a low level controller that runs on the embedded PC at a rate of 40 Hz. Instead, our controller and sensor processing algorithms run on an on-board PC that sends the velocity commands (v_X, v_Y, ω) to the MPO700 PC, via ethernet.

We have also designed three scenarios:

1) *Scenario A*: The robot navigates towards the – static – blue cart, with two obstacles (brown panels) present in the environment. The purpose of the experiment is to validate our framework when the robot has to handle simultaneously collisions and occlusions. We show in Fig. 11 the scenario as well as the images acquired by the robot left camera during navigation. The control inputs are plotted in Fig. 12. At the beginning (snapshots 1-3), since there is no risk of collision or occlusion, the robot is deviated (v_Y) and oriented (ω) so that the cameras points at the blue chariot. The first obstacle is then circumnavigated without provoking occlusions nor target loss. After that, we manually move the second obstacle in order to totally occlude the target (snapshots 4 and 5). As can be seen, the robot successfully predicts the target location, while avoiding the obstacle. Finally, when there is no more risk of collisions or occlusions, the robot converges towards the blue cart (snapshots 6-10). The evolution of the target position and orientation errors, during the navigation task, are plotted in Fig. 13. It can be seen that all three errors converge to zero as desired. As shown in Fig. 12 (and previously in Fig. 7), the control inputs generated by our controller are not smooth.

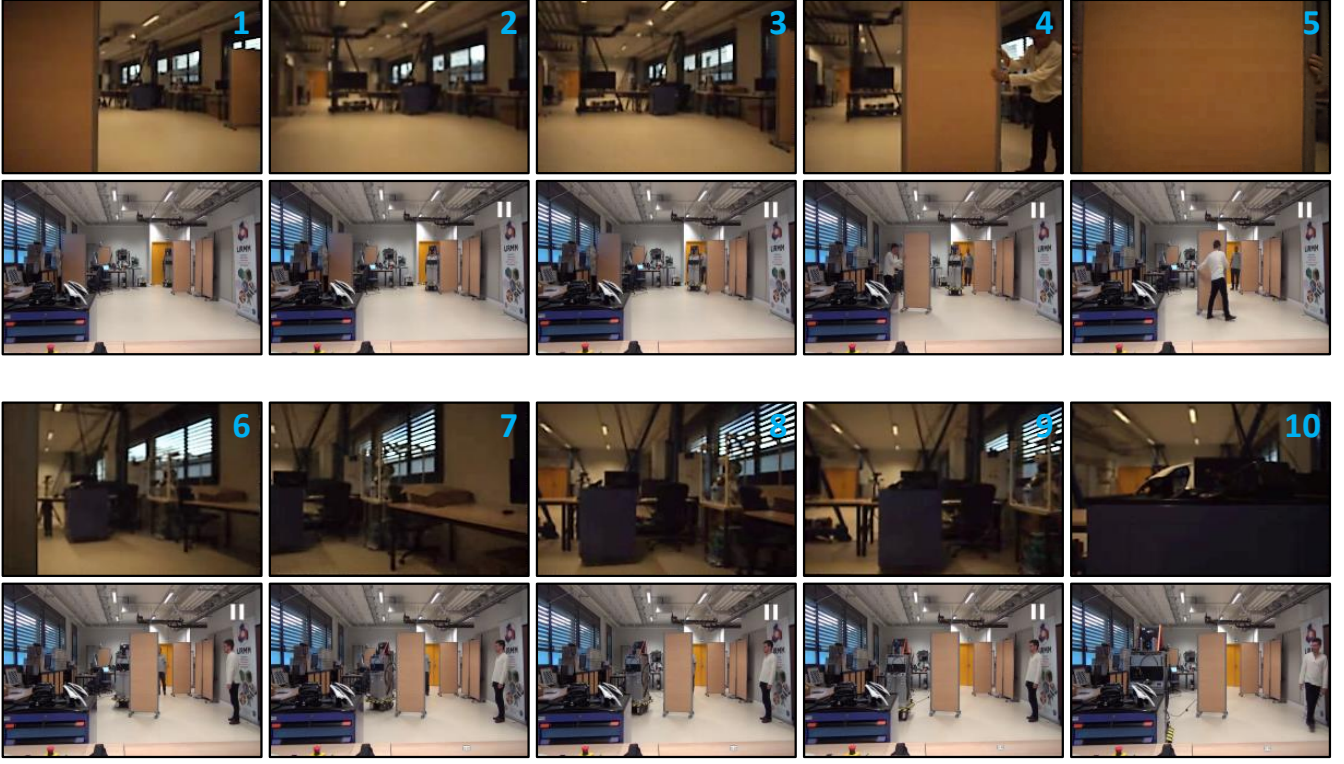


Fig. 11. Real Scenario A: the MPO700 platform navigates safely towards a static blue chariot. Top: images from the left camera, bottom: the robot (grey) avoids two obstacles while dealing with total target occlusion.

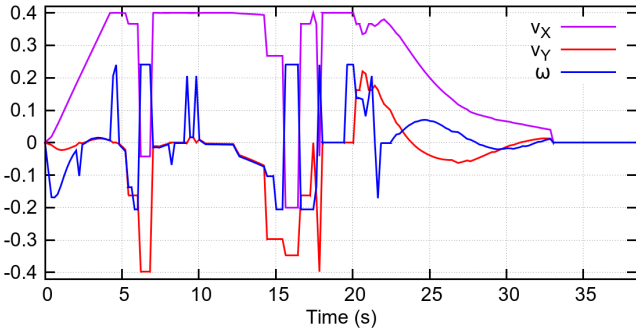


Fig. 12. Real Scenario A: MPO700 Control inputs (linear velocities v_x and v_y in m/s and angular velocity ω in rad/s).

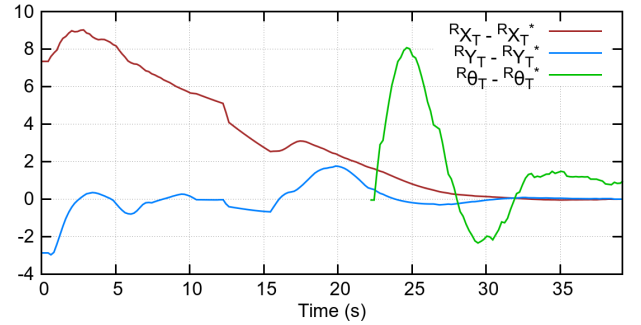


Fig. 13. Real Scenario A: evolution of position (in meters) and orientation (in degrees) errors of the target in the robot frame.

This is due to the nature of our approach, that is based on sampling a set of drivable paths. Since the sample time of our controller is higher than that of the steering wheels controller, it could be possible to filter this signal at low level. This will be done as future work.

2) *Scenario B*: In the second experiment, the navigation task consists in exploiting the omnidirectional characteristic of the robot, to follow and keep in sight a moving target, while avoiding a lateral moving obstacle (a pedestrian). As shown in Fig. 14, the robot successfully performs the visual task in spite of the walking person.

3) *Scenario C*: A final very challenging experiment was carried out to assess the robot behaviour in a complex environment, including first a corridor and then a cluttered hall (see

Fig. 15). The robot starts by following the blue chariot that is moving along the corridor (snapshots 1-4). A first moving obstacle (human) crosses the robot path and occludes the target without affecting its behaviour (snapshot 5). The robot also succeeds in avoiding a second obstacle, while following and keeping the target in its field of view until reaching the hall (snapshot 6 and 7). Then, the robot is in a difficult situation where an obstacle crosses its way, while the target has slightly changed direction (snapshot 8). This leads to a complete loss of target visibility. Once again, the robot manages to avoid the obstacle and to recover the chariot, thanks to the target pose estimation module. Finally, the robot reaches the desired pose with respect to the target (snapshots 9 and 10), after having avoided all obstacles while either keeping the target visibility



Fig. 14. Real Scenario B: lateral obstacle avoidance while maintaining the blue chariot in sight.

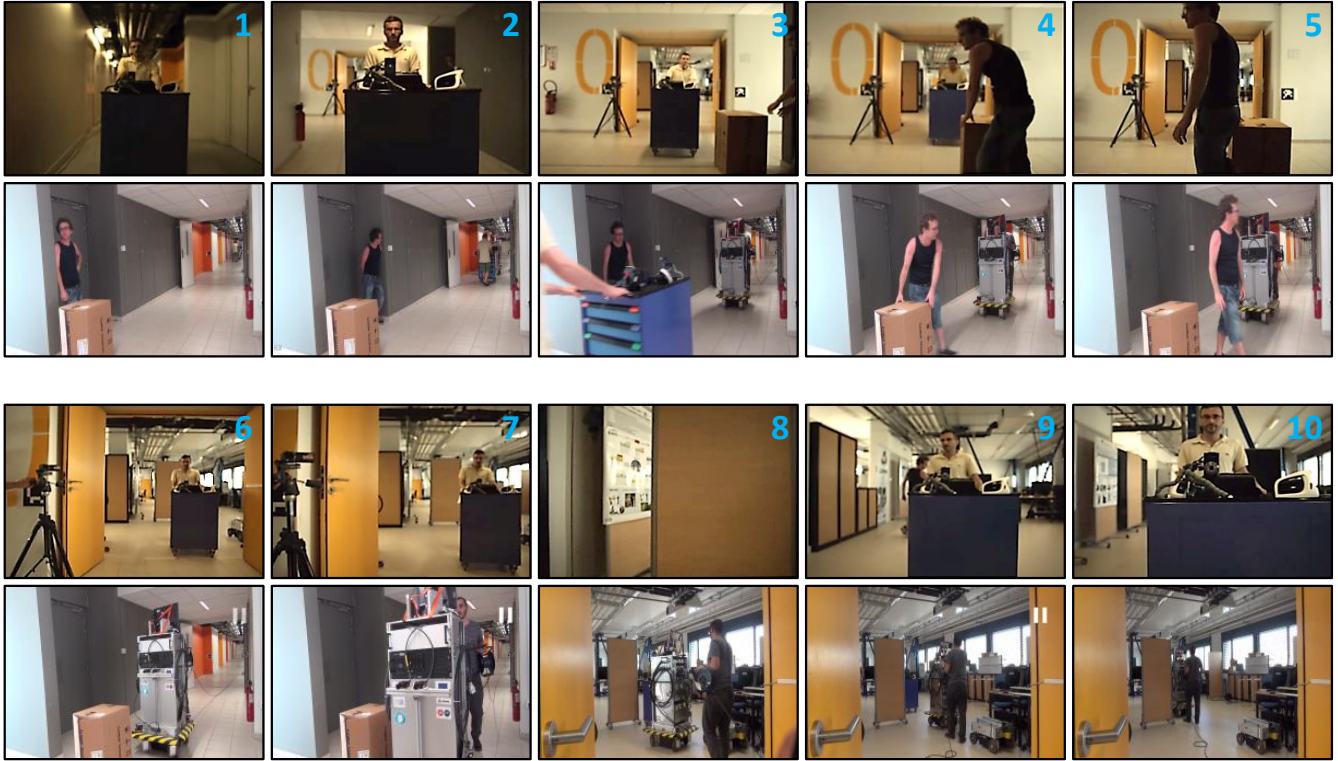


Fig. 15. Real Scenario C: the MPO700 follows a moving target in a cluttered environment, composed first of a corridor and then of a crowded hall.

or predicting its location.

VIII. CONCLUSIONS

We have presented a framework that guarantees obstacle avoidance during visual navigation of an omnidirectional robot that has to deal with visibility constraints. Additionally, the proposed framework can deal with partial and total visual occlusions provoked by the obstacles. For both perception and motion execution, we design *omnidirectional tentacles* that exploit the kinematics of the platform. Simulated and real experiments show that the robot is able to perform the task, with safety and smoothness, in spite of occlusions. Future work will investigate how to extend the proposed framework to Multi-Target Tracking (i.e., looking at multiple targets) in the presence of static and moving obstacles.

ACKNOWLEDGMENTS

This work was funded by the Algerian Ministry of Higher Education and Scientific Research and by PSA Peugeot Citroën.

REFERENCES

- [1] J. C. Latombe, "Robot motion planning", 1991, *Kluwer Academic, Dordred*.
- [2] S. M. LaValle, "Planning Algorithms", Cambridge, U.K.: Cambridge Univ. Press, 2006.
- [3] O. Khatib, "Real-time obstacle avoidance for manipulators and mobile robots", *IEEE Int. Conf. on Robotics and Automation*, 1985.
- [4] J. Borenstein and Y. Koren, "The Vector Field Histogram - Fast obstacle avoidance for mobile robots", *IEEE Trans. on Robotics and Automation*, vol. 7, no. 3, 1991, pp. 278-288.
- [5] S. Quinlan and O. Khatib, "Elastic bands: connecting path planning and control", *IEEE Int. Conf. on Robotics and Automation*, 1993.
- [6] D. Fox, W. Burgard and S. Thrun, "The Dynamic Window approach to obstacle avoidance", in *IEEE Robotics and Automation Magazine*, vol. 4, no. 1, 1997, pp. 23-33.
- [7] J. Minguez, "The Obstacle-Restriction Method (ORM) for robot obstacle avoidance in difficult environments", *IEEE/RSJ Int. Conf. on Intelligent Robots and Systems, IROS*, 2005.
- [8] M. Mujahad, D. Fischer, B. Mertsching and H. Jaddu "Closest Gap based (CG) reactive obstacle avoidance navigation for highly cluttered environments", *IEEE/RSJ Int. Conf. on Intelligent Robots and Systems, IROS*, 2010.
- [9] F. Chaumette and S. Hutchinson, "Visual servo control, Part I: Basic approaches", *IEEE Robotics and Automation Magazine*, vol. 13, no. 4, pp. 82-90, December 2006.
- [10] F. Chaumette and S. Hutchinson, "Visual servo control, Part II : Advanced approaches", *IEEE Robotics and Automation Magazine*, vol. 14, no. 1, pp. 109-118, March 2007.

- [11] D. Folio and V. Cadenat, "A redundancy-based scheme to perform safe vision-based tasks amidst obstacles", *IEEE Int. Conf. on Robotics and Biomimetics*, 2006, Kunming, China.
- [12] M. Futterlieb, V. Cadenat, T. Sentenac, "A Navigational Framework Combining Visual Servoing and Spiral Obstacle Avoidance Techniques", *Int. Conf. on Informatics in Control, Automation and Robotics (ICINCO)*, 2014.
- [13] A. Cherubini and F. Chaumette, "Visual navigation of a mobile robot with laser-based collision avoidance", *Int. Journal of Robotics Research*, vol. 32 no. 2, 2013, pp. 189–205.
- [14] A. Cherubini, F. Spindler and F. Chaumette, "A New Tentacles-based Technique for Avoiding Obstacles during Visual Navigation", *IEEE Int. Conf. on Robotics and Automation, ICRA*, 2012.
- [15] A. Cherubini, B. Grechanichenko, F. Spindler and F. Chaumette, "Avoiding moving obstacles during visual navigation", *IEEE Int. Conf. on Robotics and Automation, ICRA*, 2013.
- [16] D. Bonnafous, S. Lacroix and T. Siméon, "Motion generation for a rover on rough terrains", *IEEE/RSJ Int. Conf. on Intelligent Robots and Systems, IROS*, 2001.
- [17] F. Von Hundelshausen, M. Himmelsbach, F. Hecker, A. Mueller and H.-J. Wuensche, "Driving with tentacles-Integral structures of sensing and motion", in *Journal of Field Robotics*, 2008, vol. 25, no. 9, pp. 640–673.
- [18] Y. Mezouar and F. Chaumette, "Avoiding self-occlusions and preserving visibility by path planning in the image", *Robotics and Autonomous Systems*, vol. 41, no. 2, p. 77–87, Nov. 2002.
- [19] G. Chesi and K. Hashimoto, "Keeping features in the field of view in eye-in-hand visual servoing: a switching approach", *IEEE Trans. On Robotics*, vol. 20, no. 5, pp. 908–914, 2004.
- [20] A. Remazeilles, N. Mansard, and F. Chaumette, "Qualitative visual servoing: application to the visibility constraint", in *IEEE/RSJ Int. Conf. on Intelligent Robots and Systems, IROS*, 2006.
- [21] M. Kazemi, K. Gupta, and M. Mehrandezh, "Randomized kinodynamic planning for robust visual servoing", *IEEE Trans. on Robotics*, vol. 29, no. 5, pp. 1197–1211, 2013.
- [22] O. Kermorgant and F. Chaumette, "Dealing with constraints in sensor-based robot control", *IEEE Trans. on Robotics*, vol. 30, no. 1, pp. 244–257, 2014.
- [23] N. Cazy, P.-B. Wieber, P. R. Giordano, F. Chaumette, "Visual Servoing when Visual Information is Missing: Experimental Comparison of Visual Feature Prediction Schemes", *IEEE Int. Conf. on Robotics and Automation, ICRA*, 2015.
- [24] S. Bhattacharya, R. Murrieta-Cid, and S. Hutchinson, "Optimal paths for landmark-based navigation by differential-drive vehicles with field-of-view constraints", *IEEE Trans. on Robotics*, vol. 23, no. 1, pp. 47–59, Feb. 2007.
- [25] P. Salaris, D. Fontanelli, L. Pallottino, and A. Bicchi, "Shortest paths for a robot with nonholonomic and field-of view constraints", *IEEE Trans. on Robotics*, vol. 26, no. 2, pp. 269–280, Apr. 2010.
- [26] J. Hayet, C. Esteves, and R. Murrieta-Cid, "A motion planner for maintaining landmark visibility with a differential drive robot", in *Algorithmic Foundations of Robotics VIII*. Berlin, Germany: Springer, 2009.
- [27] J.-B. Hayet, H. Carlos, C. Esteves, and R. Murrieta-Cid, "Motion planning for maintaining landmarks visibility with a differential drive robot", *Robotics and Autonomous Systems*, vol. 62, no. 4, pp. 456–473, 2014.
- [28] D. Panagou, V. Kumar, "Cooperative visibility maintenance for leader-follower formations in obstacle environments", *IEEE Trans. on Robotics*, vol. 30, no. 4, pp. 831–844, Aug. 2014.
- [29] G. Lopez-Nicolas, N. R. Gans, S. Bhattacharya, C. Sags, J. J. Guerrero, and S. Hutchinson, "An optimal homography-based control scheme for mobile robots with nonholonomic and field-of-view constraints", *IEEE Trans. Syst., Man, Cybern. B, Cybern.*, vol. 40, no. 4, pp. 1115–1127, Aug. 2010.
- [30] D. Folio and V. Cadenat, "A sensor-based controller able to treat total image loss and to guarantee non-collision during a vision-based navigation task", in *IEEE/RSJ Int. Conf. on Intelligent Robots and Systems, IROS*, 2008.
- [31] A. Khelloufi, N. Achour, R. Passama, and A. Cherubini, "Tentacle-based moving obstacle avoidance for omnidirectional robots with visibility constraints", in *IEEE/RSJ Int. Conf. on Intelligent Robots and Systems, IROS*, 2017.
- [32] A. Cherubini, A. Crosnier, P. Fraisse, B. Navarro, R. Passama and M. Sorour, "Research on cobotics at the LIRMM IDH group", in *ICRA Workshop IC3 Industry of the future: Collaborative, Connected, Cognitive*, 2017.



Abdellah Khelloufi received the MSc in Process Control and Robotics in 2012 from the University of Sciences and Technology Houari Boumediene, Algiers. He is currently PhD student at the same university and researcher at the Center for Development of Advanced Technologies, Algiers. His research interests include robotics and computer vision, specifically vision based navigation and obstacle avoidance for mobile robots.

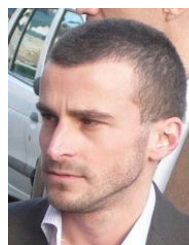


Nouara Achour is Professor at University of USTHB (Algiers). She received a degree in electronic engineering from the ENP (Ecole Nationale Polytechnique) at Algiers followed by the Magister degree in electronics applied to control processing then a PhD degree in Motion planning from USTHB University. She is Director of Research at LRPE (Laboratoire de Robotique, Parallélisme et Systèmes embarqués) at USTHB. Her main research activities deal with robotics, autonomous systems, artificial intelligence and motion planning.



robotics and medical robotics.

Robin Passama is a permanent CNRS research engineer at LIRMM since December 2012. His main research theme is software engineering for the design and development of real-time robot control architectures. He received an MSc in Computer Science in 2002 and then a PhD in Computer Science and Robotics in 2006 from the University of Montpellier. After his PhD he was involved in different European and national projects and developed applications in fields such as functional electrical stimulation, industrial robotic, fault-tolerant mobile



human-robot physical interaction, and humanoid robotics.

Andrea Cherubini received the MSc in Mechanical Engineering in 2001 from the University of Rome La Sapienza and a second MSc in Control Systems in 2003 from the University of Sheffield, U.K. In 2008, he received the PhD in Control Systems from the Dipartimento di Informatica e Sistemistica, University of Rome La Sapienza. From 2008 to 2011, he worked as post-doctoral fellow at Inria Rennes. He is currently Associate Professor at Université de Montpellier, and researcher at LIRMM. His research interests include: visual servoing for mobile robots,